Determining Bandgaps in the Layered Group-10 2D Transition Metal Dichalcogenide PtSe2

Martin Mičica, Sabrine Ayari, Minoosh Hemmat, Mehdi Arfaoui, Daniel Vala, Kamil Postava, Hadrien Vergnet, Jérôme Tignon, Juliette Mangeney, Shasha Guo, et al.

▶ **To cite this version:**

Martin Mičica, Sabrine Ayari, Minoosh Hemmat, Mehdi Arfaoui, Daniel Vala, et al.. Determining Bandgaps in the Layered Group-10 2D Transition Metal Dichalcogenide PtSe2. Advanced Functional Materials, 2024, pp.2408982. 10.1002/adfm.202408982 . hal-04753078

HAL Id: hal-04753078
https://hal.science/hal-04753078v1

Submitted on 25 Oct 2024

HAL is a multi-disciplinary open access archive for the deposit and dissemination of scientific research documents, whether they are published or not. The documents may come from teaching and research institutions in France or abroad, or from public or private research centers.

L'archive ouverte pluridisciplinaire **HAL**, est destinée au dépôt et à la diffusion de documents scientifiques de niveau recherche, publiés ou non, émanant des établissements d'enseignement et de recherche français ou étrangers, des laboratoires publics ou privés.

Distributed under a Creative Commons Attribution - NonCommercial - NoDerivatives 4.0 International License

ADVANCED FUNCTIONAL MATERIALS
www.afm-journal.de

Determining Bandgaps in the Layered Group-10 2D Transition Metal Dichalcogenide $PtSe_2$

Martin Mičica, Sabrine Ayari, Minoosh Hemmat, Mehdi Arfaoui, Daniel Vala, Kamil Postava, Hadrien Vergnet, Jerome Tignon, Juliette Mangeney, Shasha Guo, Xuechao Yu, Qi Jie Wang, Zheng Liu, Sihem Jaziri, Francesca Carosella, Robson Ferreira, and Sukhdeep Dhillon**

Unlike traditional group-6 transition metal dichalcogenides (TMDs), group-10 TMDs such as $PtSe_2$ and $PdTe_2$ possess highly tuneable indirect bandgaps, transitioning from semiconducting in the near-infrared to semimetal behavior with a number of monolayers (MLs). This opens up the possibility of TMD-based mid-infrared and terahertz optoelectronics. Despite this large potential, the optical properties of such materials have shown an extremely large disparity between that predicted and measured. For example, simulations show that a few MLs is required for the semiconductor–semimetal transition, whilst tens of MLs is found experimentally. This is a result of widely used optical extrapolation methods to determine bandgaps, such as the Tauc plot approach, that are not adapted here owing to i) nearby direct transitions, ii) the material dimensionality and iii) large changes in the non-parabolic bandstructure with MLs. Here, uniquely combining optical ellipsometry to determine the complex permittivity, terahertz time resolved spectroscopy for the complex conductivity and in-depth density functional theory (DFT) simulations, it is shown that the optical properties and bandstructure can be determined reliably and demonstrate clearly that the semiconductor-semimetal transition occurs for $PtSe_2$ layers ≈5 MLs. The microscopic origins of the observed transitions and the crucial role of the Coulomb interaction for thin semiconducting layers, and that of interlayer van der Waals forces for multilayer semimetallic samples are also demonstrated. This work of combining complimentary experimental techniques and extensive simulations avoids the application of constrained extrapolation methods to determine the optical properties of group-10 TMDs, and will be of importance for future mid-infrared and terahertz applications.

1. Introduction

2D layered transition metal dichalcogenides (TMDs) have garnered considerable interest, offering distinct electronic and optical properties compared to their bulk counterparts.[1,2] These materials possess intrinsic characteristics such as layered crystallinity and weak van der Waals (vdW) molecular bonding, whilst their optoelectronic properties can be controlled based on their layer-dependent electronic band structure.[3–5] Group-10 TMDs,[6,7] such as $PtSe_2$.[8] stand out for uniquely containing a noble metal (e.g., Pt) instead of the more commonly studied materials such as MoS_2 and WSe_2 (Group-6 TMDs). Although relatively less explored, group-10 TMDs offer some important characteristics in photonics and optoelectronics. As well as a higher mobility than other TMDs and air-stability,[9] group 10 TMDs have a stronger interlayer coupling that leads to large variations in their electronic bandgap with the number of atomic layers. This interesting behavior allows for extremely large tunability of the indirect bandgap in, for example, $PtSe_2$, ranging from 1.2 eV for a monolayer to zero (semimetallic) as the number of layers increases (**Figure 1**),[10,11] as well as large changes in the non-parabolic bandstructure form.[12,13] This renders the material particularly interesting for mid-infrared (MIR) and terahertz (THz) science and applications,[14] compared to other TMDs that are limited to the optical or near-infrared range as the bandgap does not significantly change with number of layers. Recent examples have shown, for example, layer dependent atmospheric stable mid-infrared detectors,[15,16] THz pulse

The ORCID identification number(s) for the author(s) of this article can be found under https://doi.org/10.1002/adfm.202408982

© 2024 The Author(s). Advanced Functional Materials published by Wiley-VCH GmbH. This is an open access article under the terms of the Creative Commons Attribution-NonCommercial-NoDerivs License, which permits use and distribution in any medium, provided the original work is properly cited, the use is non-commercial and no modifications or adaptations are made.

DOI: 10.1002/adfm.202408982

M. Mičica, S. Ayari, M. Hemmat, M. Arfaoui, H. Vergnet, J. Tignon, J. Mangeney, F. Carosella, R. Ferreira, S. Dhillon
Laboratoire de physique de l'Ecole Normale Supérieure (LPENS), ENS
Université PSL, CNRS
Sorbonne Université
Université Paris Cité
Paris 75005, France
E-mail: martin.micica@phys.ens.fr; sukhdeep.dhillon@phys.ens.fr

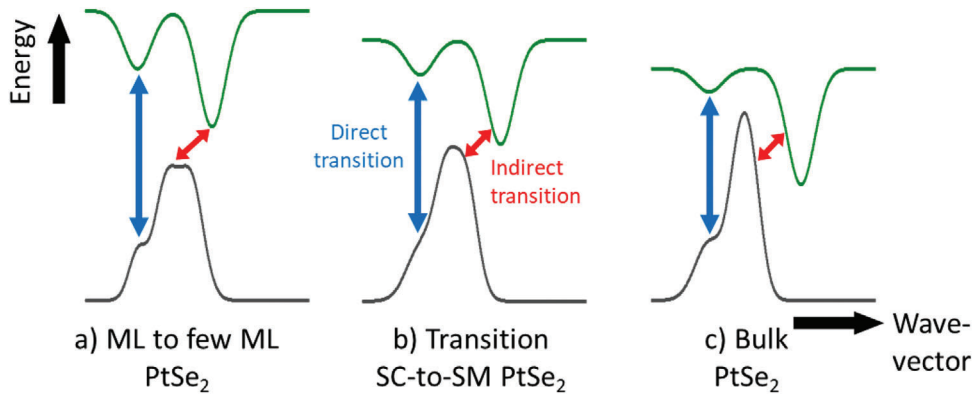

Figure 1. Schematic of the bandstructure and the presence of direct and indirect bandgaps in the Group 10 TMD $PtSe_2$. A large tunability in the gap energy is possible with the number of layers, ranging from a) semiconducting (SC) for a ML or few ML, b) SC-to-SM transition for several ML, to c) semimetallic (SM) behavior for bulk $PtSe_2$ as the number of layers increases. A grand disparity in the number of layers for b) the SC-SM transition has been reported. Direct and indirect (i.e., assisted) optical transitions can in principle coexist for all configurations.

generation[17–19] and THz spintronic emitters[20] to name a few.

Despite the strong interest and promising technological applications of group-10 2D TMDs, there remains considerable discrepancies in the reported measured and simulated optical properties of these materials, and in particular the number of layers required for the semiconductor to semimetal (SC–SM) transition and the excitonic nature of the former. Indeed:

i) Band structure simulations based on density functional theory (DFT) reveal a bandgap energy that decreases fast with increasing thickness and vanishes for typically a few MLs. However, there is little a consensus on the number of layers for the SC–SM transition, which depends in particular on the model used for the vdW interaction.[10,21,22]
ii) Experimentally, contradictory reports exist with much slower decrease of gap energy with thickness, such as the findings of Wang et al.[23] or Xie et al.,[24] showing $PtSe_2$ with tens of monolayers that still exhibits semiconductor behavior when the standard Tauc method (see below) is employed.

Regarding the second point, these types of experimental results have also been seen in other group-10 2D TMDs.[25] The methods used are based on extrapolating the measured optical losses from high energies to the intercept of the energy axis with a form depending on the bandgap type. This widespread strategy for bandgap measurement is based on the phenomenological law for the optical loss:

$$\alpha = A \times (h\nu - E_g)^r \times Y[h\nu - E_g] \quad (1)$$

where $h\nu$ is the photon energy, E_g is the bandgap, A is a proportionality constant, $Y[X]$ is the step function (= 0 for $X < 0$ and = 1 for $X > 1$), and α is the sample absorption (or absorption coefficient for thick enough samples). The parameter r is such that $\alpha^{1/r}$ plotted as a function of $h\nu$ presents a linear behavior over a large enough energy interval above the bandgap, allowing the determination of E_g by a linear extrapolation toward vanishing absorption, as schematically shown in **Figure 2**. This experimental protocol is very general and has been used in many different situations, related each to a specific r value: direct or indirect bandgaps, involving dipolar or defect-assisted (by static[26] and phonon (see e.g.,[27]) transitions, and for systems with different dimensionalities (2D, 3D). Indeed, the critical exponent r is closely related to the microscopic origin of the absorption. For instance, for parabolic conduction and valence bands, and for dipolar transitions in direct bandgaps in dimension d, one has:

$$r = (d - 2)/2 \quad (2)$$

M. Arfaoui, S. Jaziri
Laboratoire de Physique de la Matière Condensée
Département de Physique
Faculté des Sciences de Tunis
Université Tunis El Manar
Campus Universitaire, Tunis 1060, Tunisie
D. Vala, K. Postava
Department of Materials Engineering and Recycling
Faculty of Materials Science and Technology
VSB-Technical University of Ostrava
17. listopadu 2172/15, Ostrava-Poruba 708 00, Czech Republic
S. Guo, Z. Liu
School of Materials Science and Engineering
Nanyang Technological University
50 Nanyang Avenue, Singapore 639798, Singapore
X. Yu
Key Laboratory of Multifunctional Nanomaterials and Smart Systems
Suzhou Institute of Nano-Tech and Nano-Bionics
Chinese Academy of Sciences
Jiangsu, Suzhou 215123, China
Q. J. Wang
School of Electrical and Electronic Engineering & School of Physical and Mathematical Sciences
The Photonics Institute
Nanyang Technological University
50 Nanyang Avenue, Singapore 639798, Singapore
S. Jaziri
Faculté des Sciences de Bizerte
Laboratoire de Physique des Matériaux: Structure et Propriétés
Université de Carthage
Bizerte, Jarzona 7021, Tunisie

© 2024 The Author(s). Advanced Functional Materials published by Wiley-VCH GmbH

RIGHTSLINK
16163028, 0, Downloaded from https://onlinelibrary.wiley.com/doi/10.1002/adfm.202408982 by Cochrane France, Wiley Online Library on [25/10/2024]. See the Terms and Conditions (https://onlinelibrary.wiley.com/terms-and-conditions) on Wiley Online Library for rules of use; OA articles are governed by the applicable Creative Commons License

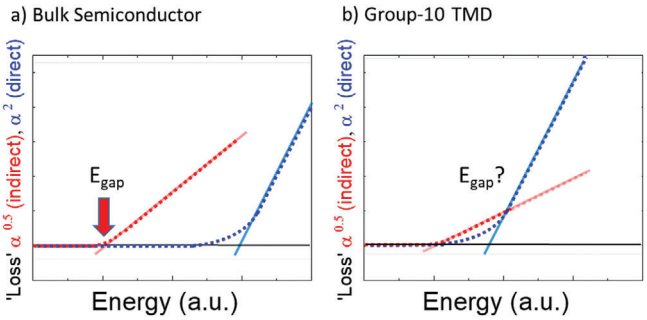

Figure 2. Ideal cases of optical losses as a function of energy for indirect ($\alpha^{1/2}$ red dotted lines) and direct (α^2, blue dotted line) transitions to determine the energy gap via extrapolating the absorption function to cross the energy axis (solid lines) for a) classic bulk semiconductors (e.g., Si) where the indirect and direct transitions are largely separated in energy and b) Group 10 TMDs where the indirect and direct transitions are close in energy and where the use of extrapolation methods to determine the bandgap are difficult to reliably apply.

resulting in a linear extrapolation of the form α^2 for bulk materials (blue curve), while for assisted transitions in bulk 3D indirect bandgap materials one has:[27]

$$r = 2 \tag{3}$$

resulting in a linear extrapolation of $\alpha^{1/2}$ (red curve of Figure 2). To further illustrate the roles of the microscopic process of interest and of the system dimensionality on the value of r, consider the generic case of an indirect bandgap material with conduction and valence dispersions $E_c(\boldsymbol{k})$ and $E_v(\boldsymbol{k})$ (with $\boldsymbol{k}$ a d-dimensional vector) that can be non-parabolic around their extrema: $E_c = E_g + \alpha_c \mid \boldsymbol{k} - \boldsymbol{k}_c \mid^{\nu}$ and $E_v = -\alpha_v k^{\mu}$ for the conduction and valence bands, respectively, where ν and μ are arbitrary non-vanishing constants. This represents a simple description of bulk germanium or silicon cases for $\nu = \mu = 2$ and $d = 3$. Following the same main assumptions for assisted transitions that lead to the well known value $r = 2$, one can then obtain (see Supporting Information):

$$r = d(1/\nu + 1/\mu) - 1 \tag{4}$$

This general result simplifies to $r = 2$ for bulk ($d = 3$) and parabolic ($\nu = \mu = 2$) dispersions, and the extrapolation (the so-called Tauc plot method) has proven to be reliable to determine bandgaps in classic bulk semiconductors (e.g., silicon). However, for indirect 2D materials, this application of $r = 2$ is not pertinent. Even if $d = 2$ is fixed for not too thick $PtSe_2$ multilayers, the r-value for assisted transitions can still vary considerably with the layer number, owing to the important non-parabolicity of the bands (as shown schematically in Figure 1 and in the Supporting Information that presents the calculated band structures of various multilayers). Additionally, compared to silicon where the indirect and direct transitions are clearly separated (Figures 1a and 2a), the proximity and the spectral overlap of direct to indirect transitions in group-10 TMD multilayers (Figures 1b,c and 2b) render such extrapolation procedure meaningless. Despite these applicability limits owing to non-parabolicity, close direct transitions and rapid bandstructure changes, the value $r = 2$ has been used in several works to extract E_g in 2D TMD films.[23,24] This has resulted in disparate reporting of the SC–SM transition to be tens of MLs and strongly hampers the application of these materials to photonic and optoelectronic applications.

This work provides a comprehensive experimental and theoretical study of the optical properties of the group-10 2D TMD $PtSe_2$ over a range of layers thicknesses and an extremely wide spectral range. Experiments run from the UV to the THz range using UV–Vis–NIR ellipsometry and terahertz time domain spectroscopy (THz TDS). Ab-initio calculations allows to investigate a range of different interactions to identify the underlying physical phenomena that determine the $PtSe_2$ properties. This permits the linear optical properties and bandgaps of $PtSe_2$ to be reliably determined experimentally and theoretically, showing a SC–SM transition ≈5–6 ML without relying on unjustified and unadapted extrapolation protocols. In fact, by correlating the experimental dielectric function with the underlying band structure, we show the prominent role of the Coulomb interaction in semiconductor $PtSe_2$, and vdW couplings in semi-metal multilayers.

The work is structured as follows. The samples are described and standard characterization (atomic force microscopy [AFM] and Raman) permits the sample thickness and number of MLs to be determined. Transmittance experiments provide a first discrimination between SC and SM layers, in particular in the long wavelength region. Ellipsometry measurements then allow to extract the complex permittivity spectrum, which is compared to theoretical DFT calculations. DFT calculations combined with the Bethe–Salpeter equation (BSE) for semiconducting $PtSe_2$ show exciton features from strong direct interband transitions. This is followed by THz conductivity measurements confirming the semiconductor to semimetal transition determined via ellipsometry and DFT.

2. Experimental Section

The samples of $PtSe_2$ were prepared by thermally assisted conversion. The process consists of the preparation of a thin layer of metal, platinum in the case, by magnetron sputtering on a fused quartz substrate, followed by conversion of platinum into $PtSe_2$ in a heated selenium gas atmosphere.[8,23] The final thickness of the prepared $PtSe_2$ film depends on the thickness of prepared platinum layer. By this method wafer scale $PtSe_2$ are produced with high uniformity over large surface areas. Both AFM (for atomic thickness calibration) and Raman (to show the presence and quality of $PtSe_2$) measurements were performed. A summary of the AFM data is shown in **Figure 3**a, highlighting a thickness with selenization ratio of 5.5 between the primary deposited platinum film and final grown $PtSe_2$ film. The linear response with the Pt thickness shows that in the range of thicknesses investigated the conversion efficiency of Pt to $PtSe_2$ remains constant. XPS spectra on samples using the same growth method has evidenced no unselenized Pt[28,29]). The uniformity and surface quality for the thickest layer of $PtSe_2$ appear to decrease, possibly owing to the accumulation of growth defects, and shows the limit of $PtSe_2$ thicknesses using this growth method. The Raman analysis performed by a Renishaw inVia microscope (Figure 3b)) shows Raman modes characteristic for $PtSe_2$ in-plane E_g (≈175 cm^{-1}), out-of-plane A_{1g} (≈205 cm^{-1}), and LO (≈230 cm^{-1}) vibrations,

© 2024 The Author(s). Advanced Functional Materials published by Wiley-VCH GmbH

RIGHTSLINK
16163028, 0, Downloaded from https://onlinelibrary.wiley.com/doi/10.1002/adfm.202408982 by Cochrane France, Wiley Online Library on [25/10/2024]. See the Terms and Conditions (https://onlinelibrary.wiley.com/terms-and-conditions) on Wiley Online Library for rules of use; OA articles are governed by the applicable Creative Commons License

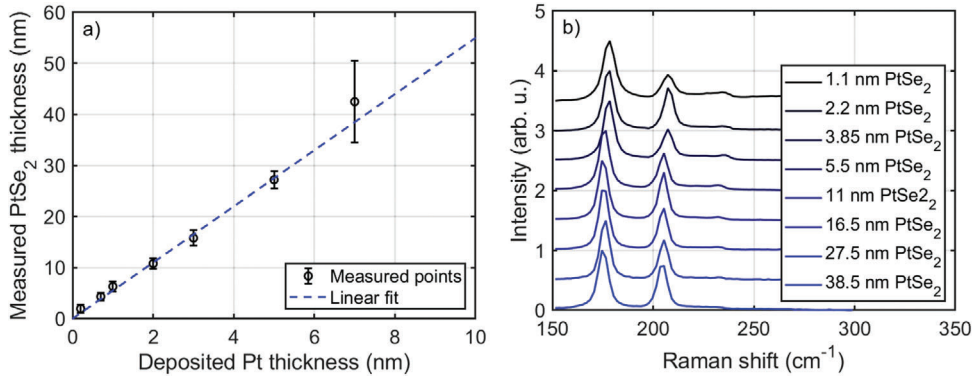

Figure 3. Characterization of grown $PtSe_2$ layers. a) Thickness of $PtSe_2$ layers obtained from AFM as a function of their deposited Pt thickness shown by black circles. The linear fit reveals a conversion factor of 5.5 nm of $PtSe_2$ per nm of Pt. b) Raman spectra for different thicknesses of $PtSe_2$ films. Spectra are offset for clarity.

and where the center frequency changes corresponding to the change in the thickness.[30] Summarized results on the samples are presented in **Table 1**.

3. Results

3.1. Optical Transmission and Ellipsometry - UV–Vis–NIR Characterization

To determine the optical properties of $PtSe_2$ samples in the UV–Vis–NIR region, transmission spectroscopy and spectroscopic ellipsometry were used. A dual beam spectrometer Agilent Cary 7000 was employed to measure transmission spectra under normal incidence in the spectral region 175–3500 nm with a clean substrate placed in the reference beam path. The obtained transmittance displayed as solid lines in **Figure 4** shows two dominant features: the first ≈400 nm which is present in all samples and undergoes a redshift with increasing thickness of $PtSe_2$ layer, and the second that starts to be noticeable for the 2.2 nm sample close to 750 nm and undergoes a redshift up to 860 nm for the 27.5 nm $PtSe_2$ sample. In the longer NIR region, $PtSe_2$ itself does not show any absorption peaks, and features in the region centered at 2700 nm originate from the substrate. The transmittance per layer of the three thickest samples differ by less than 0.04 (and by less than 0.002 for wavelengths longer than ≈2 μm), indicating a bandstructure that no longer evolves significantly with thickness beyond 10 ML. These thick structures display a sizeable absorption that decreases slowly with decreasing energy and is roughly proportional to the sample thickness for long wavelengths; the origin of this loss and calculated transmission is discussed below. Thin samples display an important layer-dependent transmittance and negligible loss in the long wavelength region: in particular, the 4 ML absorption rapidly decreases to zero ≈1 eV, suggesting it still a SC. Note that applying the $r = 2$ extrapolation approach discussed above to our transmission measurements also results in an incorrect determination of the bandgap closing at tens of MLs, as observed by previous studies.

Table 1. Summary of sample characterization via AFM and Raman spectroscopy. The columns from left to right are the deposited Pt thickness, the measured thickness of the $PtSe_2$ layer obtained, the number of layers, the in-plane E_g and out-of-plane A_{1g} frequency vibrations.

Pt (nm)	$PtSe_2$ (nm)	# layers	E_g (cm^{-1})	A_{1g} (cm^{-1})
0.1	0.55 ± 0.34	1	–	–
0.2	1.1 ± 0.76	2 ± 1	179.22 ± 0.33	208.48 ± 0.66
0.4	2.2 ± 0.8	4 ± 1	178.28 ± 0.30	208.27 ± 0.16
0.7	3.85 ± 0.82	7 ± 1	177.50 ± 0.15	207.30 ± 0.11
1	5.5 ± 1.02	10 ± 2	175.30 ± 0.06	205.19 ± 0.06
2	11 ± 1.06	20 ± 2	174.56 ± 0.04	204.86 ± 0.08
3	16.5 ± 1.5	29 ± 3	174.67 ± 0.11	204.75 ± 0.06
5	27.5 ± 1.7	49 ± 3	174.44 ± 0.12	204.75 ± 0.11
7	38.5 ± 8	69 ± 14	175.88 ± 1.30	205.32 ± 0.77

More precise information on the complex permittivity (and hence complex refractive index) was obtained by variable angle spectroscopic ellipsometry (Mueller matrix spectroscopic ellipsometer Woollam RC2-DI) with measurements in spectral range 193–1700 nm and angles ranging from 55° to 75° with 5° steps. This technique is extremely sensitive to determine the optical properties of thin films and can be applied to TMDs.[31] Obtained results were fitted by Kramers–Kronig consistent complex permittivity model[32] containing the infinity term $\varepsilon_\infty = 1$ and three Lorentz oscillators:

$$\tilde{\varepsilon} = \varepsilon' + i\varepsilon'' = 1 + \sum_{j=1}^{3} \frac{Amp_j Br_j En_j}{En_j^2 - E^2 - iEBr_j} \quad (5)$$

The resulting complex permittivity (real part ε' and imaginary part ε''), is displayed in **Figure 5**, and best-fitted parameters are attached in Table SI (Supporting Information). It is important to note that the prepared TMD samples are isotropic in the plane owing to its polycrystalline nature, as reported in previous studies on $PtSe_2$.[24] The out-of-plane anisotropy is discussed below. Notice finally that thin (up to 2.2 nm) and thick samples can be roughly grouped together, with regards to the gross spectral variations of their measured permittivity, in good correspondence with the previously mentioned qualitative distinction of thin and thick samples regarding their low energy transmittance spectra (Figure 4). Moreover, at long wavelengths ε'' is roughly

© 2024 The Author(s). Advanced Functional Materials published by Wiley-VCH GmbH

RIGHTSLINK

16163028, 0, Downloaded from https://onlinelibrary.wiley.com/doi/10.1002/adfm.202408982 by Cochrane France, Wiley Online Library on [25/10/2024]. See the Terms and Conditions (https://onlinelibrary.wiley.com/terms-and-conditions) on Wiley Online Library for rules of use; OA articles are governed by the applicable Creative Commons License

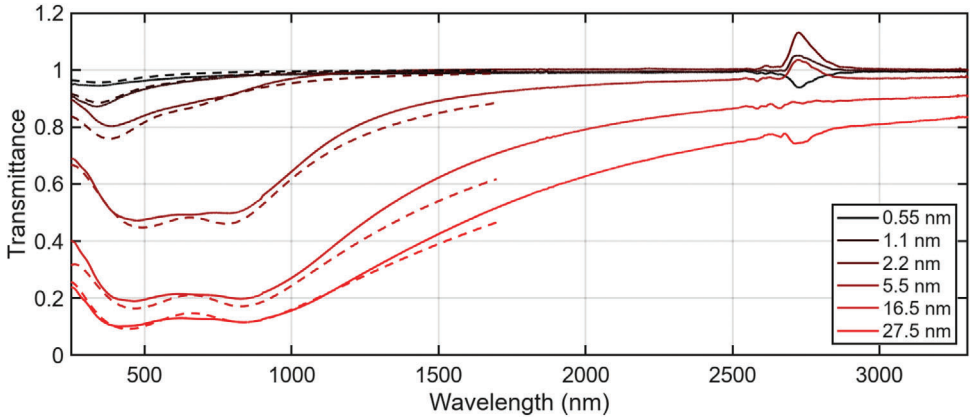

Figure 4. Optical transmission under normal incidence for different $PtSe_2$ thicknesses extracted over the UV, visible, and near-infrared spectral regions, referenced to the clean substrate (solid lines). Features ≈2700 nm originates from impurities and variation of fused quartz substrates. Calculated transmission for normal incidence (dashed lines).

thickness-independent for thick layers, in agreement with the linear increase with layers number of the loss in transmission experiments (Figure 4). The large difference in the optical constants for 38.5 nm $PtSe_2$ compared to other thick samples is a result of the decrease of the uniformity and surface quality for the thickest layer of $PtSe_2$ as shown in the AFM measurements.

Previous investigations of ellipsometry of $PtSe_2$[33,34] have shown similar position of the oscillators but with slightly different permittivity. This could be a result of the different growth technique and sample preparation used, and the different substrates used as proximity effects play a key role in the optical properties of 2D materials

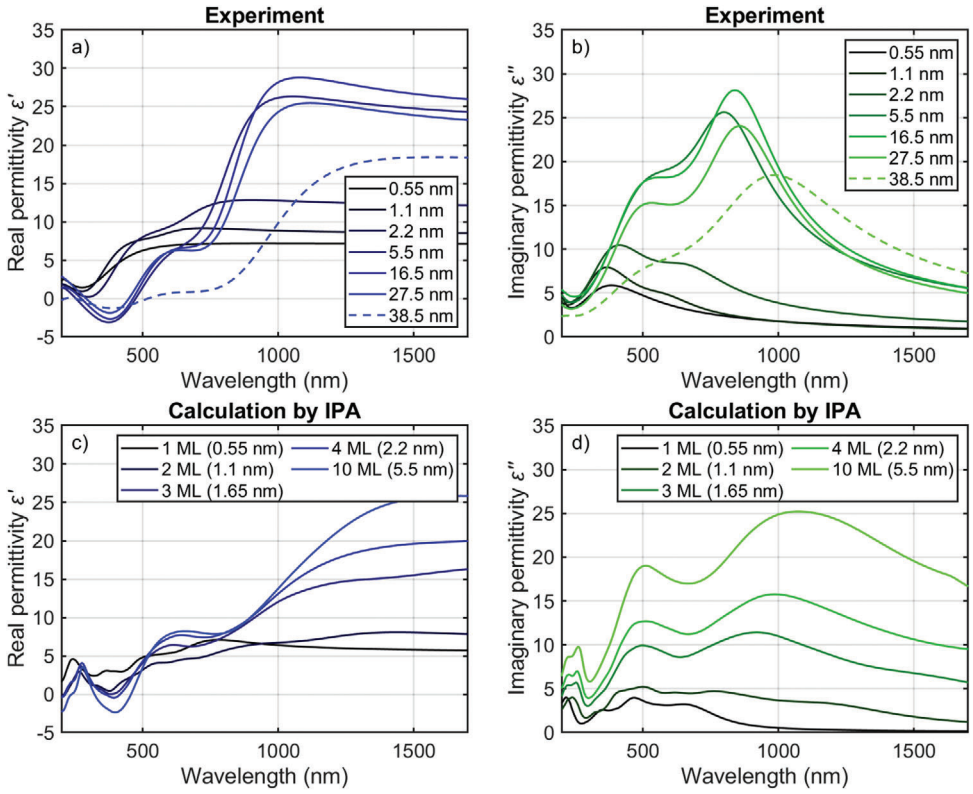

Figure 5. Spectra obtained from ellipsometry measurements of $PtSe_2$ of a) real ε' and b) imaginary ε'' permittivity of $PtSe_2$ with different thicknesses. Measurements for 38.5 nm (dashed lines) show a change in position of oscillators as well as in amplitude when compared with slightly thinner samples, which could be a result of a larger inhomogeneity for the thickest sample (see AFM measurements Figure 3). Figure c) and d) show the calculated real and imaginary permittivities, respectively, from DFT simulations (GGA-TS - IPA with a phenomenological broadening $\gamma = 0.2$ eV).

© 2024 The Author(s). Advanced Functional Materials published by Wiley-VCH GmbH

RIGHTSLINK

16163028, 0, Downloaded from https://onlinelibrary.wiley.com/doi/10.1002/adfm.202408982 by Cochrane France, Wiley Online Library on [25/10/2024]. See the Terms and Conditions (https://onlinelibrary.wiley.com/terms-and-conditions) on Wiley Online Library for rules of use; OA articles are governed by the applicable Creative Commons License

3.2. Modeling of the Layer-Dependent Optical Properties and Bandstructure

In this section, we investigate simulation of the transmission, the permittivities and the bandstructure, and compare to the experimental results. The calculated transmission for the various samples is shown in the dashed lines of Figure 4. The transmission is calculated as $T = \frac{|t_{012}|^2}{|t_{02}|^2}$ where t_{012} and t_{02} are the complex Fresnel transmission coefficients, at normal incidence, respectively for a three layers (air/film/substrate) and a two layers (air/substrate) system (see e.g.,[35]). The complex refractive index of the $PtSe_2$ material in t_{012} is taken from the ellipsometry measurements. (The absence of results beyond roughly 1700 nm is a result of the limitations of the ellipsometry spectral range). The very good agreement reveals the high consistency of the two experiments.

The permittivities were obtained from first principles DFT calculations, showing that several experimental spectral features and tendencies can be microscopically correlated to interband optical transitions. To this end, we use different levels of approximation to evaluate the electronic states: the generalized gradient approximation (GGA), the quasiparticle GW method that allows a better account of the electron–electron interactions The permittivity is evaluated in the dipolar approximation whether within the independent particle approximation (IPA) or for excitonic transitions using the GW plus Bethe Salpeter equation (GW-BSE) approach. (See the Supporting Information for more details). The numerical complexity increases considerably from GGA to GW and then to GW-BSE methods. However, as we discuss below, the appropriate model is dictated by the number of layers: the excitonic framework is needed to describe thin SC layers, while thick SM ones can be described by the GGA model with good enough accuracy. The role of the vdW interactions is discussed below. To take into account the in- and out-of plane anisotropy, we calculate the average permittivity: $\tilde{\varepsilon}(\omega) = \cos^2(\theta)\tilde{\varepsilon}_{xx}(\omega) + \sin^2(\theta)\tilde{\varepsilon}_{zz}(\omega)$, where $\theta = 65°$. This choice gives a better general agreement with the experimental results, as it allows to account to some extent for the fact that the ellipsometry measurements were done with different angles ranging from 55° to 75°. In all permittivity simulations we have used a phenomenological energy broadening $\gamma = 0.2$ eV.

One point of particular interest in the measured permittivity is that its real part becomes negative for thick layers (greater than 2.2 nm) ≈400 nm in wavelength. This feature of ε' can be attributed to the dielectric response of high energy transitions in $PtSe_2$, similar as in metals (e.g. Ag,[36] Al[37]) or in semiconductors (e.g. GaAs,[38,39] GaSb[40]). The consideration of this feature has permitted us to refine our model description. In fact, the calculated electronic dispersions and optical properties of multilayers TMDs strongly depend on the used vdW model. To incorporate vdW interactions, a large number of methods have been proposed.[41–48] We have realized extensive band structure (GGA) and permittivity (GGA-IPA) calculations using 10 different models: DFT-D, DFT-D2, DFT-D3, VdW-DF1, VdW-DF2, VdW-DF3, VdW-DF-C6, EMD, rvv10 and TS. (Figures S7 and S9, and Table SII, Supporting Information show the effect of different vdW models on $PtSe_2$ electronic dispersions, for a 4 ML structure). The first 8 models are inappropriate in our case: the first three predict a semi-metallic behavior already for the 2 ML and/or 3 ML case, whereas the next five cannot account for the measured sign changing of ε' ≈400 nm (See Figure S8, Supporting Information). The latter behavior can be obtained using the last two models, rVV10 and TS, which actually predict very close band structures and permitivities. Here, we choose to retain the TS model. Note finally that a DFT calculation without any vdW coupling similarly cannot explain the permittivity behavior ≈400 nm. In conclusion, as shown in Figure 5, the behavior of ε' ≈400 nm is excellently reproduced by our DFT calculations within the TS model (Figure 5c,d). The GGA-TS model predicts a vanishing of the electronic bandgap ≈4 ML. However, as we discuss below, corrections beyond the GGA approach raises the bandgap of thin samples, rendering the 4 ML sample a small-gap SC, in agreement with the measured behaviors observed for the permittivities of thick and thin samples at long wavelengths. To summarise, we obtain a close match to the transmittance and ellipsometry experiments, permitting to range the SC–SM transition to be slightly greater than 4 ML. Additionally, as we show later below, it is further corroborated by experiments of conductivity in the THz region allowing to fine tune this value. For the moment, we consider the measured and calculated real and imaginary permittivities (ε', ε''), which exhibit a large variation with $PtSe_2$ thickness, in particular the relative intensities and the peak energy positions. We will show the origin of these variations and the nature of the electronic excitations behind the peaks i.e., interband or excitonic origin. (Figure S1, Supporting Information shows the single-particle electronic band structure of $PtSe_2$ as a function of film thickness).

Although there is generally a good agreement of the main spectral features between theory and experiment for thick layers in Figure 5 (≥10), thinner layers appear to be spectrally blue-shifted in the experimental data. Different effects can be at the origin of the disagreement, such as the disorder derived from structural imperfections or local strain, the environment or exciton coupling. Here, we will focus on one intrinsic effect, namely on the role of beyond-GGA corrections and exciton coupling on the optical spectra (i.e. using the GW-BSE approach[49–52]). Indeed, it is well known that such corrections and excitonic coupling may drastically affect the interband transitions of a semiconducting material. **Figure 6**a,c shows the simulated permittivity ε'' for 1 and 2 ML $PtSe_2$, respectively, using two different models, which allow us to elucidate the relative importance of the excitonic effect. Compared to the experimental data, the simulations using IPA are considerably red-shifted, which shows that the ground state calculation performed by DFT methods fails to reproduce the actual energy excitation spectra. The implementation of the BSE method on top of the quasi-particle GW approximation leads to an improved agreement with the measurements, highlighting the importance of the direct electron–hole interaction that drives the exciton formation and leads to a dramatic rearrangement of the spectral response. To further illustrate the importance of excitons for very thin layers, we calculate a binding energy of the lowest exciton as high as 0.5 eV for 1 ML, which decreases to 0.2 eV for 2 ML.

Finally, for comparison, the simulated permittivity for 10 ML $PtSe_2$ obtained using the IPA approach is shown in Figure 6e). We observe again a red-shift of the GGA-IPA main peak as compared to the experiments, which is nevertheless much smaller than those for 1 and 2 ML. This may be due

© 2024 The Author(s). Advanced Functional Materials published by Wiley-VCH GmbH

RIGHTSLINK
16163028, 0, Downloaded from https://onlinelibrary.wiley.com/doi/10.1002/adfm.202408982 by Cochrane France, Wiley Online Library on [25/10/2024]. See the Terms and Conditions (https://onlinelibrary.wiley.com/terms-and-conditions) on Wiley Online Library for rules of use; OA articles are governed by the applicable Creative Commons License

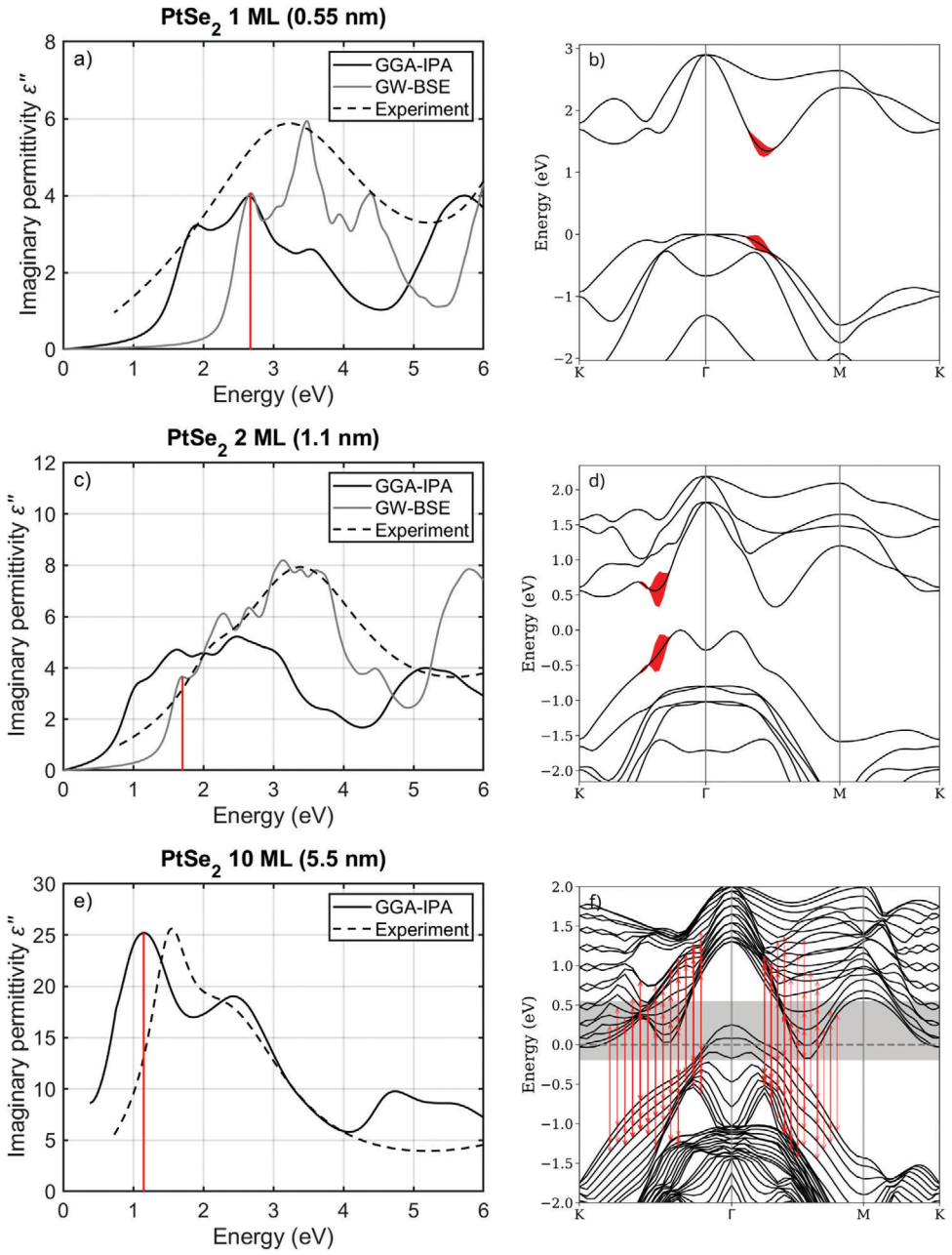

Figure 6. Comparison of the experimental (dashed lines) and calculated (full lines) imaginary permittivity ε'' of the complex dielectric function $\tilde{\varepsilon}$ for a) 1 ML, b) 2 ML and c) 10 ML $PtSe_2$. For 1 and 2 ML the GGA-IPA and GW-BSE modellings are compared. Band structures for the b) 1 ML, d) 2 ML and f) 10 ML samples (GGA-TS model), respectively. The red shaded areas in b) and d) visualize the single-particle states that contribute the most to the formation of the exciton state responsible for the peak transition marked by a red vertical bar in a) and c). The vertical bars in f) show the interband transitions the most contributing to the main peak marked by the vertical bar in e).

to residual coulombs interactions affecting the high-energy transitions.

To better understand the underlying band structure origin of the optical transitions responsible for the high-energy absorption spectra of very thin (1 ML, 2 ML) and thick (10 ML) samples, i.e. representative cases of SC and SM behaviors, respectively, we plot in Figure 6b,d,f, the valence and conduction states contributing the most to the optical absorption peak marked by a red bar in Figure 6a,c,e, projected onto the $K-\Gamma-M-K$ band diagram. Let us start considering the thickest sample (SM case of 10 ML). In Figure 6f) the direct interband transitions contributing the most to the first absorption peak are highlighted by red bars on the bandstructure along various k-space directions. In more detail, the CB and VB states involved in such transitions are joined by a grey bar presenting a resonant or near-resonant (±0.2 eV) photon absorption and with sizeable optical matrix element $\langle \phi_{c,k}|p_\alpha|\phi_{v,k}\rangle$ (where p_α is the momentum operator along the α direction and $\phi_{n,k}$ the Bloch states). It is clear that the main

© 2024 The Author(s). Advanced Functional Materials published by Wiley-VCH GmbH

RIGHTSLINK

16163028, 0, Downloaded from https://onlinelibrary.wiley.com/doi/10.1002/adfm.202408982 by Cochrane France, Wiley Online Library on [25/10/2024]. See the Terms and Conditions (https://onlinelibrary.wiley.com/terms-and-conditions) on Wiley Online Library for rules of use; OA articles are governed by the applicable Creative Commons License

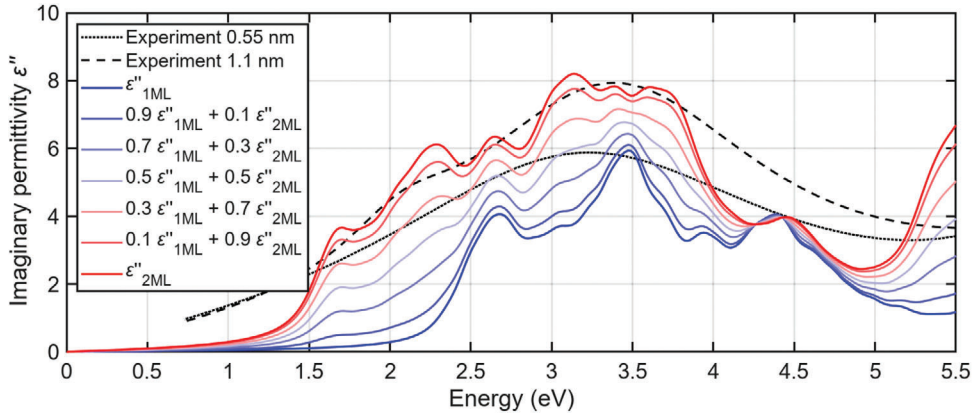

Figure 7. Comparison of imaginary part of the effective permittivity for different fractions f of 1 and 2 ML $PtSe_2$.

peak involves a large number of VB-to-CB transitions, dispersed over a large fraction of the Brillouin zone. (In Figure S10, Supporting Information, we also plot a 2D k-resolved spectra over the whole Brillouin zone.) This feature is a clear signature of the 2D - to - 3D dimensional transition for increasing sample thickness.

For thin layers, the red shaded areas in Figure 6b,d present the exciton weights of the exciton state responsible for the first interband transition (marked by a red bar in the corresponding GW-BSE spectrum in Figure 6a,b). The weights quantify the contributions of different VB and CB states to a specific exciton state (for each exciton state the total weight over the whole Brillouin zone is normalized to unity; see Supporting Information for more details). When projected onto the single-particle electronic band diagram, as in Figure 6d,e, the weights provide intuitive information on the underlying initial and final single-electron states involved in a given excitonic interband transition. For 1 ML (2 ML), the fundamental excitonic peak in $\epsilon''(\omega)$, at energy ≈2.8 eV (1.8 eV), comes from states of the first valence and conduction bands located at roughly midpoint on the $\Gamma - M$ ($\Gamma - K$) line. Although the binding energy of the fundamental exciton of 1 ML is ≈2.5 larger than that of 2 ML, their k-space extensions (size of the shaded regions) are quite similar. Interestingly, for 1 and 2 ML, the set of valence and conduction states, which contribute the most to the first interband IPA transition, largely overlaps with the set of states that predominately contribute to the formation of the exciton state responsible for the fundamental BSE transition. The 2D k-resolved spectra to identify the origin of the peaks for the GGA-IPA methods are shown in Figure S10 (Supporting Information), as well as the method to determine the exciton wavefunction and exciton weights.

Although including excitonic effect enhances the comparison results, there is still a shift between experiment and theory for the 1 ML case. This is mainly due to the lower quality and uniformity of the 1 ML sample, which also contains a fraction of 2 ML regions. Indeed, assuming that the sample is composed of an inhomogeneous distribution of regions of either 1 ML or 2 ML thicknesses (large enough to be properly described by their bulk properties, but much smaller than the excitation spot), the resulting effective permittivity $\tilde{\varepsilon}_{\text{eff}}$ can be approximated by the effective medium approximation of two parallel mediums with complex permittivities $\tilde{\varepsilon}_{1\text{ML}}$ and $\tilde{\varepsilon}_{2\text{ML}}$,[35]

$$\tilde{\varepsilon}_{\text{eff}} = f\,\tilde{\varepsilon}_{1\text{ML}} + (1-f)\,\tilde{\varepsilon}_{2\text{ML}} \tag{6}$$

with f the fraction of 1 ML regions. **Figure 7** presents the transition of the imaginary permittivity from 1 to 2 ML, when changing the fraction f of 1 ML, in the effective medium and compared to experimental measurements. Including 0.5 fraction of 2 ML substantially improves the agreement with the measurement of 0.55 nm thick $PtSe_2$ sample. Further increasing the fraction of 2 ML up to 1 shows convergence to the measurement result of 1.1 nm $PtSe_2$, showing better overall agreement with the theoretical results and growth quality of the sample.

For low energies, the measured weak but sizeable absorptions may prove detrimental to possible optoelectronic applications aiming at exploring the high real index of such materials. For the thinnest layers, the observed residual loss (Figure 5b) extending well below the first absorption peak may be imputed to the moderate (2 ML) or low (1 ML) optical quality of the samples, which may for instance contain small amount of residual Pt. For thick samples, both theoretical and experimental results demonstrate an important and slowly decreasing absorption tail. It is, however, important to mention that the principal peak does not correspond to the fundamental interband direct transitions, as illustrated by the Figure 6f). Indeed, for 10 ML the latter transition occurs at much smaller energy, i.e., near 0.3 eV, as shown in **Table 2**. This table shows more generally the layers variations of different calculated transition energies of interest: the direct bandgap in the GGA–TS approach, and the edges of the indirect interband transitions for both GGA–TS and GW–TS models. For reference, the lowest accessible energies in our ellipsometry spectroscopy and transmittance experiments occur at ≈0.7 and 0.37 eV, respectively. Thus, for all thick layers (≥10 ML) the measurements fall in the spectral region were direct transitions are present. Indirect (i.e., assisted by disorder) absorption is in principle also possible in this same spectral region but is expected to dominate the absorption at much lower energies, i.e., below the direct bandgap edge, but can extend toward higher energies, overlapping the direct transitions, as schematically shown in Figure 1. However, owing to the good agreement with the simulations, one may infer a much smaller contribution of the indirect transitions

© 2024 The Author(s). Advanced Functional Materials published by Wiley-VCH GmbH
RIGHTSLINK
16163028, 0, Downloaded from https://onlinelibrary.wiley.com/doi/10.1002/adfm.202408982 by Cochrane France, Wiley Online Library on [25/10/2024]. See the Terms and Conditions (https://onlinelibrary.wiley.com/terms-and-conditions) on Wiley Online Library for rules of use; OA articles are governed by the applicable Creative Commons License

Table 2. Direct and indirect electronic bandgaps for different layers of $PtSe_2$ in eV calculated at the DFT/PBE level accounting for the TS vdW interaction and using many body perturbation theory (GW).

–	GGA–TS		GW–TS
N ML	E_g^{dir} (eV)	E_g^{indir} (eV)	E_g^{indir} (eV)
1 ML	1.53	1.35	2.55
2 ML	0.96	0.35	1.33
3 ML	0.72	0.08	0.9
4 ML	0.65	−0.09	0.3
5 ML	0.49	−0.19	0.04
6 ML	0.43	−0.27	–
7 ML	0.38	−0.33	–
8 ML	0.36	−0.36	–
9 ML	0.32	−0.39	–
10 ML	0.3	−0.41	–

at the experimentally investigated energies. Finally, notice that for thick layers the indirect bandgap becomes negative and smoothly decreases to a value near the bulk one (≈−0.5 eV[10,19]).

To conclude this section, we show that a SC–SM transition ≈5–6 ML can be reliably inferred from a careful analysis of the transmittance and permittivity data, and confrontation with a modeling properly accounting for the excitonic and vdW couplings, without relying on unadapted extrapolation protocols. We show in the following that conductivity in the THz region additionally corroborates these findings.

3.3. Conductivity in THz Region

The above showed the response of $PtSe_2$ in the optical domain and suggests that the semiconductor to semimetal transition occurs for layers slightly greater than 4 ML. To further support this conclusion, in the following the response of $PtSe_2$ is studied at frequencies, frequencies i.e., at low photon energies and with time-domain spectroscopy. This method has been proven to be ideally adapted to measuring the conductivity of thin film materials.[53] The complex conductivity $\tilde{\sigma}(\omega)$,

$$\tilde{\sigma}(\omega) = \sigma'(\omega) + i\sigma''(\omega) \tag{7}$$

is investigated utilizing a custom-built THz time-domain spectroscopy (TDS) system with usable bandwidth from 250 GHz to 2.5 THz. By measuring the $\tilde{\sigma}(\omega)$, a clear change should be observed when the $PtSe_2$ transits from semiconductor to semimetal. Here, we extract $\tilde{\sigma}(\omega)$ from a single measurement of $PtSe_2$ on the substrate using a self-referenced THz-TDS method.[54] In this case, the incident THz beam that passes through the thin film of $PtSe_2$ on the substrate undergoes internal reflections, leading to time echoes, delayed in time compared to the directly transmitted pulse. **Figure 8**a shows the transmitted pulse and the reflected pulse with a separation of 10 ps corresponding to the thickness of the substrate. However, as a function of number of layers, their amplitudes as well as their time separation from the main pulse are different, suggesting different conductivities.

The directly transmitted pulse and the transient from the first echo (or three single-passes inside the sample) can be used to determine the complex conductivity of the thin films. Following the approach of self-referenced TDS,[54] the frequency-dependent conductivity of our measured $PtSe_2$ films, $\tilde{\sigma}_{PtSe_2}(\omega)$ is given by:

$$\tilde{\sigma}_{PtSe_2}(\omega) = \frac{\left(\tilde{n}_{sub} - 1\right)^2 \Delta\tilde{p}_{sub}(\omega) - \left(\tilde{n}_{sub} + 1\right)^2 \tilde{T}(\omega)}{Z_0\left(\left(\tilde{n}_{sub} + 1\right)\tilde{T}(\omega) + \left(\tilde{n}_{sub} - 1\right)\Delta\tilde{p}_{sub}(\omega)\right)} \tag{8}$$

$\tilde{T}$ is the transmission function defined as the ratio of the first echo relative to the directly transmitted pulse. The term $\Delta\tilde{p}$ is the propagation factor difference that takes into account the phase shift due to the additional round trip in the substrate, Gouy phase correction introduced by the THz-focused beam on the sample,[55] and amplitude correction caused by the absorption of the substrate. $\tilde{n}_{sub}$, was estimated by measuring the distance between the two peaks in the frequency domain and the thickness of the substrate ($\tilde{n}_{sub} = c/d_{sub}.f_p$). The latter determined the refractive index of our substrate to be $\tilde{n}_{sub} = 1.95$, which is approximately constant in the considered spectral range.[56] Z_0 is the vacuum impedance. Figure 8b shows both the real (line) and imaginary

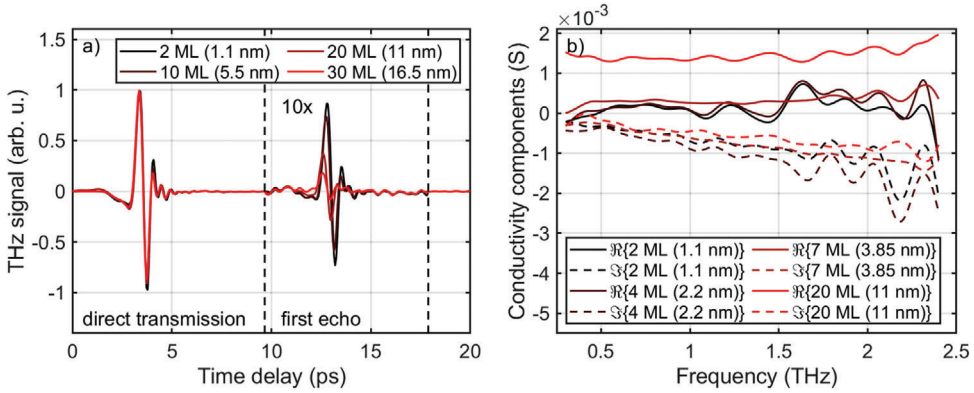

Figure 8. THz time-domain spectroscopy of $PtSe_2$ layers. a) THz transmission signal in time-domain measured for different thicknesses of samples: 2 ML (1.1 nm), 10 ML (5.5 nm), 20 ML (11 nm), and 30 ML (16.5 nm) $PtSe_2$. The THz pulse transmitted directly and its first echo from the first internal reflections are also shown. The amplitude of the pulse from the internal reflection is enlarged by 10 times for clarity. b) Real and imaginary parts of the optical conductivity spectra of a selection of $PtSe_2$ samples in the THz domain shown by straight and dashed lines, respectively.

© 2024 The Author(s). Advanced Functional Materials published by Wiley-VCH GmbH

RIGHTSLINK
16163028, 0, Downloaded from https://onlinelibrary.wiley.com/doi/10.1002/adfm.202408982 by Cochrane France, Wiley Online Library on [25/10/2024]. See the Terms and Conditions (https://onlinelibrary.wiley.com/terms-and-conditions) on Wiley Online Library for rules of use; OA articles are governed by the applicable Creative Commons License

(dashed line) calculated conductivity of four different $PtSe_2$ thicknesses, including the thinnest and thickest layers. (The measurements show slight fluctuations due to this self-referenced approach and the noise initially present in the time traces). As can be observed the conductivity is approximately constant for 2 and 4 ML, whilst an increase is seen for 7 ML $PtSe_2$, followed by a jump for 20 ML $PtSe_2$. The observed increase in conductivity then suggests that the transition from semiconductor to semimetal for layers between 5 and 7 ML, similar to the ellipsometry measurements presented above, and again largely smaller than the Tauc plot approach for indirect group 10 TMDs.

4. Conclusion

To conclude, this work has presented a careful and reliable approach to determining the optical properties of 2D materials based on a Group-10 element of the periodic table, which have previously shown large disparities. We used ellipsometry to determine the dielectric function, which was in good agreement with DFT calculations, suggesting that the semiconducting-semimetal transition occurs for ≈5 ML $PtSe_2$ and not tens of ML as previous optical measurements.[23,24] The experiment-modeling confrontation highlights the different interactions that need to be taken into account. For very thin semiconducting $PtSe_2$ the Couloumb coupling is of paramount importance, showing the appearance of marked exciton signatures. A proper account of interlay vdW coupling is necessary to describe the multilayer optical properties. The approach permitted to microscopically correlate the spectral signatures in the experimental dielectric function to features of the multilayer band structure and interband transitions. We further show that the traditional plot extrapolation approaches needs to be handled with care in these materials. These considerably underestimates the bandgap values owing to the presence of strong direct transitions close in energy to the indirect transition and the non-parbolic layer-dependent bandstructure. Finally, we show that THz TDS is also a complimentary means to determine the conductive nature of the films and hence the semiconductor-semimetal transition. This work is particularly important as the group-10 TMDs are promising for MIR and THz technologies owing to a highly tuneable bandgap, and reliable knowledge of the bandgap is vital for further progress in their photonic, nonlinear and optoelectronic applications.

Supporting Information

Supporting Information is available from the Wiley Online Library or from the author.

Acknowledgements

M.M., S.A., and M.H. contributed equally to this work. The authors acknowledge funding from European Union's Horizon 2020 research and innovation program under grant agreement No 964735 (FET-OPEN EXTREME-IR). This work was supported by a government grant managed by the ANR as part of the France 2030 investment plan from PEPR SPIN ANR-22-EXSP-0002. Z.L. acknowledges the funding support from the National Research Foundation Singapore under CRP program (Grant No. NRF-CRP26-2021-0004). X.Y. is grateful for the technical support from the Nano-X from Suzhou Institute of Nano-Tech and Nano-Bionics, Chinese Academy of Sciences (SINANO). This work was granted access to the HPC resources of MesoPSL financed by the Region Ile de France and the project EquipMeso (reference ANR-10-EQPX-29-01) of the programme Investissements d'Avenir supervised by the Agence Nationale pour la Recherche. K. Postava and D. Vala acknowledge No. CZ.02.01.01/00/22_008/0004631-"Materials and Technologies for Sustainable Development," funded by the European Union and the state budget of the Czech Republic within the framework of the Jan Amos Komensky Operational Program, and RE-FRESH - Research Excellence For Region Sustainability and High-tech Industries project number CZ.10.03.01/00/22_003/0000048 via the Operational Programme Just Transition.

Conflict of Interest

The authors declare no conflict of interest.

Data Availability Statement

The data that support the findings of this study are available from the corresponding author upon reasonable request.

Keywords

2D materials, density functional theory, group-10 transition metal dichalcogenides, optical spectroscopy, terahertz

Received: May 24, 2024
Revised: September 3, 2024
Published online:

[1] S. Manzeli, D. Ovchinnikov, D. Pasquier, O. V. Yazyev, A. Kis, *Nat. Rev. Mater.* **2017**, *2*, 17033.
[2] C. Tan, X. Cao, X.-J. Wu, Q. He, J. Yang, X. Zhang, J. Chen, W. Zhao, S. Han, G.-H. Nam, M. Sindoro, H. Zhang, *Chem. Rev.* **2017**, *117*, 6225.
[3] C. Yim, N. McEvoy, S. Riazimehr, D. S. Schneider, F. Gity, S. Monaghan, P. K. Hurley, M. C. Lemme, G. S. Duesberg, *Nano Lett.* **2018**, *18*, 1794.
[4] Q. H. Wang, K. Kalantar-Zadeh, A. Kis, J. N. Coleman, M. S. Strano, *Nat. Nanotechnol.* **2012**, *7*, 699.
[5] C. Palacios-Berraquero, M. Barbone, D. M. Kara, X. Chen, I. Goykhman, D. Yoon, A. K. Ott, J. Beitner, K. Watanabe, T. Taniguchi, A. C. Ferrari, M. Atatüre, *Nat. Commun.* **2016**, *7*, 1.
[6] E. Chen, W. Xu, J. Chen, J. Warner, *Mater. Today Adv.* **2020**, *7*, 100076.
[7] L. Pi, L. Li, K. Liu, Q. Zhang, H. Li, T. Zhai, *Adv. Funct. Mater.* **2019**, *29*, 1904932.
[8] Y. Wang, L. Li, W. Yao, S. Song, J. Sun, J. Pan, X. Ren, C. Li, E. Okunishi, Y.-Q. Wang, E. Wang, Y. Shao, Y. Zhang, H.-T. Yang, E. F. Schwier, H. Iwasawa, K. Shimada, M. Taniguchi, Z. Cheng, S. Zhou, S. Du, S. J. Pennycook, S. T. Pantelides, H.-J. Gao, *Nano Lett.* **2015**, *15*, 4013.
[9] Y. Zhao, J. Qiao, Z. Yu, P. Yu, K. Xu, S. P. Lau, W. Zhou, Z. Liu, X. Wang, W. Ji, Y. Chai, *Adv. Mater.* **2017**, *29*, 1604230.
[10] R. A. B. Villaos, C. P. Crisostomo, Z.-Q. Huang, S.-M. Huang, A. A. B. Padama, M. A. Albao, H. Lin, F.-C. Chuang, *npj 2D Mater. Appl.* **2019**, *3*, 2.
[11] Y. Gong, Z. Lin, Y.-X. Chen, Q. Khan, C. Wang, B. Zhang, G. Nie, N. Xie, D. Li, *Nano-Micro Lett.* **2020**, *12*, 174.
[12] G. Liu, Z. Cui, F. Zhang, Y. Zeng, W. Chen, Y. Liu, Z. Nie, Q. Bao, *Small Sci.* **2023**, *3*, 2300030.

© 2024 The Author(s). Advanced Functional Materials published by Wiley-VCH GmbH

16163028, 0, Downloaded from https://onlinelibrary.wiley.com/doi/10.1002/adfm.202408982 by Cochrane France, Wiley Online Library on [25/10/2024]. See the Terms and Conditions (https://onlinelibrary.wiley.com/terms-and-conditions) on Wiley Online Library for rules of use; OA articles are governed by the applicable Creative Commons License

[13] S. Aas, C. Bulutay, *J. Appl. Phys.* **2019**, *126*, 115701.
[14] A. Leitenstorfer, A. S. Moskalenko, T. Kampfrath, J. Kono, E. Castro-Camus, K. Peng, N. Qureshi, D. Turchinovich, K. Tanaka, A. G. Markelz, M. Havenith, C. Hough, H. J. Joyce, W. J. Padilla, B. Zhou, K.-Y. Kim, X.-C. Zhang, P. U. Jepsen, S. Dhillon, M. Vitiello, E. Linfield, A. G. Davies, M. C. Hoffmann, R. Lewis, M. Tonouchi, P. Klarskov, T. S. Seifert, Y. A. Gerasimenko, D. Mihailovic, R. Huber, et al., *J. Phys. D: Appl. Phys.* **2023**, *56*, 223001.
[15] N. Sefidmooye Azar, J. Bullock, V. R. Shrestha, S. Balendhran, W. Yan, H. Kim, A. Javey, K. B. Crozier, *ACS Nano* **2021**, *15*, 6573.
[16] X. Yu, P. Yu, D. Wu, B. Singh, Q. Zeng, H. Lin, W. Zhou, J. Lin, K. Suenaga, Z. Liu, Q. J. Wang, *Nat. Commun.* **2018**, *9*, 1.
[17] L. Zhang, D. Zhang, F. Hu, X. Xu, Q. Zhao, X. Sun, H. Wu, Z. Lü, X. Wang, Z. Zhao, *Adv. Opt. Mater.* **2022**, *11*, 2201881.
[18] L. Cheng, Y. Xiong, L. Kang, Y. Gao, Q. Chang, M. Chen, J. Qi, H. Yang, Z. Liu, J. C. Song, E. E. M. Chia, *Sci. Adv.* **2023**, *9*, eadd7856.
[19] M. Hemmat, S. Ayari, M. Mičica, H. Vergnet, S. Guo, M. Arfaoui, X. Yu, D. Vala, A. Wright, K. Postava, J. Mangeney, F. Carosella, S. Jaziri, Q. J. Wang, Z. Liu, J. Tignon, R. Ferreira, E. Baudin, S. Dhillon, *InfoMat* **2023**, *5*, e12468.
[20] K. Abdukayumov, M. Mičica, F. Ibrahim, L. Vojáček, C. Vergnaud, A. Marty, J.-Y. Veuillen, P. Mallet, I. G. de Moraes, D. Dosenovic, S. Gambarelli, V. Maurel, A. Wright, J. Tignon, J. Mangeney, A. Ouerghi, V. Renard, F. Mesple, J. Li, F. Bonell, H. Okuno, M. Chshiev, J.-M. George, H. Jaffrès, S. Dhillon, M. Jamet, *Adv. Mater.* **2024**, *36*, 2304243.
[21] L. Ansari, S. Monaghan, N. McEvoy, C. Ó. Coileáin, C. P. Cullen, J. Lin, R. Siris, T. Stimpel-Lindner, K. F. Burke, G. Mirabelli, Ray Duffy, Enrico Caruso, Roger E. Nagle, G. S. Duesberg, P. K. Hurley, F. Gity, *npj 2D Mater. Appl.* **2019**, *3*, 33.
[22] A. Kandemir, B. Akbali, Z. Kahraman, S. Badalov, M. Ozcan, F. İyikanat, H. Sahin, *Semicond. Sci. Technol.* **2018**, *33*, 085002.
[23] L. Wang, S. Zhang, N. McEvoy, Y.-y. Sun, J. Huang, Y. Xie, N. Dong, X. Zhang, I. M. Kislyakov, J.-M. Nunzi, L. Zhang, J. Wang, *Laser Photonics Rev.* **2019**, *13*, 1900052.
[24] J. Xie, D. Zhang, X.-Q. Yan, M. Ren, X. Zhao, F. Liu, R. Sun, X. Li, Z. Li, S. Chen, Z.-B. Liu, J.-G. Tian, *2D Mater.* **2019**, *6*, 3.
[25] M. Wei, J. Lian, Y. Zhang, C. Wang, Y. Wang, Z. Xu, *npj 2D Mater. Appl.* **2022**, *6*, 1.
[26] J. Tauc, *Mater. Res. Bull.* **1968**, *3*, 37.
[27] M. C. Peter, Y. Yu, *Fundamentals of Semiconductors Physics and Materials Properties*, Springer, New York **1997**.
[28] Y. He, L. Liu, C. Zhu, S. Guo, P. Golani, B. Koo, P. Tang, Z. Zhao, M. Xu, C. Zhu, P. Yu, X. Zhou, C. Gao, X. Wang, Z. Shi, L. Zheng, J. Yang, B. Shin, J. Arbiol, H. Duan, Y. Du, M. Heggen, R. E. Dunin-Borkowski, W. Guo, Q. J. Wang, Z. Zhang, Z. Liu, *Nat. Catal.* **2022**, *5*, 212.
[29] S. Lukas, O. Hartwig, M. Prechtl, G. Capraro, J. Bolten, A. Meledin, J. Mayer, D. Neumaier, S. Kataria, G. S. Duesberg, M. C. Lemme, *Adv. Funct. Mater.* **2021**, *31*, 2102929.
[30] M. O'Brien, N. McEvoy, C. Motta, J.-Y. Zheng, N. C. Berner, J. Kotakoski, K. Elibol, T. J. Pennycook, J. C. Meyer, C. Yim, M. Abid, T. Hallam, J. F. Donegan, S. Sanvito, G. S. Duesberg, *2D Mater.* **2016**, *3*, 2.
[31] G.-H. Jung, S. Yoo, Q.-H. Park, *Nanophotonics* **2018**, *8*, 263.
[32] J.A.Woollam Co., *CompleteEASE Software Manual*, J.A. Woollam, Lincoln, NE, USA **2014**, p. 356.
[33] G. A. Ermolaev, K. V. Voronin, M. K. Tatmyshevskiy, A. B. Mazitov, A. S. Slavich, D. I. Yakubovsky, A. P. Tselin, M. S. Mironov, R. I. Romanov, A. M. Markeev, I. A. Kruglov, S. M. Novikov, A. A. Vyshnevyy, A. V. Arsenin, V. S. Volkov, *Nanomaterials* **2021**, *11*, 12.
[34] J. He, W. Jiang, X. Zhu, R. Zhang, J. Wang, M. Zhu, S. Wang, Y. Zheng, L. Chen, *Phys. Chem. Chem. Phys.* **2020**, *22*, 26383.
[35] H. Fujiwara, *Spectroscopic Ellipsometry: Principles and Applications*, 1st ed., John Wiley & Sons, Hoboken, New Jersey **2007**.
[36] H. U. Yang, J. D'Archangel, M. L. Sundheimer, E. Tucker, G. D. Boreman, M. B. Raschke, *Phys. Rev. B* **2015**, *91*, 235137.
[37] D. Gérard, S. K. Gray, *J. Phys. D: Appl. Phys.* **2014**, *48*, 184001.
[38] A. D. Rakić, M. L. Majewski, *J. Appl. Phys.* **1996**, *80*, 5909.
[39] S. Lai, W. Wu, W. Gu, *J. Nanomater.* **2015**, *2015*, 897542.
[40] M. Muñoz, K. Wei, F. H. Pollak, J. L. Freeouf, G. W. Charache, *Phys. Rev. B* **1999**, *60*, 8105.
[41] S. Grimme, *J. Comput. Chem.* **2004**, *25*, 1463.
[42] A. D. Becke, E. R. Johnson, *J. Chem. Phys.* **2007**, *127*, 15.
[43] A. Otero-De-La-Roza, E. R. Johnson, *J. Chem. Phys.* **2012**, *136*, 17.
[44] A. Tkatchenko, M. Scheffler, *Phys. Rev. Lett.* **2009**, *102*, 073005.
[45] M. Dion, H. Rydberg, E. Schröder, D. C. Langreth, B. I. Lundqvist, *Phys. Rev. Lett.* **2004**, *92*, 246401.
[46] K. Lee, É. D. Murray, L. Kong, B. I. Lundqvist, D. C. Langreth, *Phys. Rev. B* **2010**, *82*, 081101.
[47] D. Chakraborty, K. Berland, T. Thonhauser, *J. Chem. Theory Comput.* **2020**, *16*, 5893.
[48] R. Sabatini, T. Gorni, S. De Gironcoli, *Phys. Rev. B* **2013**, *87*, 041108.
[49] G. Strinati, *Riv. Nuovo Cimento (1978-1999)* **1988**, *11*, 1.
[50] G. Onida, L. Reining, A. Rubio, *Rev. Mod. Phys.* **2002**, *74*, 601.
[51] K. S. Thygesen, *2D Mater.* **2017**, *4*, 022004.
[52] A. Marini, C. Hogan, M. Grüning, D. Varsano, *Comput. Phys. Commun.* **2009**, *180*, 1392.
[53] H. J. Joyce, J. L. Boland, C. L. Davies, S. A. Baig, M. B. Johnston, *Semicond. Sci. Technol.* **2016**, *31*, 103003.
[54] P. R. Whelan, Q. Shen, D. Luo, M. Wang, R. S. Ruoff, P. U. Jepsen, P. Bøggild, B. Zhou, *Opt. Express* **2020**, *28*, 28819.
[55] P. Kužel, H. Němec, F. Kadlec, C. Kadlec, *Opt. Express* **2010**, *18*, 15338.
[56] E. Dadrasnia, S. Puthukodan, V. V. Thalakkatukalathil, H. Lamela, G. Ducournau, J.-F. Lampin, F. Garet, J.-L. Coutaz, *J. Spectrosc.* **2014**, *2014*, 601059.

© 2024 The Author(s). Advanced Functional Materials published by Wiley-VCH GmbH

RIGHTSLINK

16163028, 0, Downloaded from https://onlinelibrary.wiley.com/doi/10.1002/adfm.202408982 by Cochrane France, Wiley Online Library on [25/10/2024]. See the Terms and Conditions (https://onlinelibrary.wiley.com/terms-and-conditions) on Wiley Online Library for rules of use; OA articles are governed by the applicable Creative Commons License